# Low-Power Quadrature Receivers for ZigBee (IEEE 802.15.4) Applications

Marika Tedeschi, *Member, IEEE*, Antonio Liscidini, *Member, IEEE*, and Rinaldo Castello, *Fellow, IEEE*

***Abstract*—Two very compact and low power quadrature receivers for ZigBee applications are presented. Area and power savings are obtained through both current reuse and oscillator tank sharing between the I and Q paths. Since this choice can cause I and Q amplitude/phase mismatches, the conversion gain is analyzed and a technique to minimize these errors is implemented. Moreover, since using a single tank makes quadrature generation at the local oscillator level costly and power-hungry, two alternative quadrature generation techniques in the RF path are proposed, together with the corresponding input matching strategies.**

**Two 90 nm CMOS receiver prototypes that implement the above strategies were designed and integrated. The measurements resulted in a power consumption of 3.6 mW and an active die area of 0.23 mm$^2$ when the LNA is separated from the self-oscillating mixer and high quality factor bond-wire inductors are used in the *LC* tank. The active area increases to 0.35 mm$^2$ when the LNA is stacked with the self-oscillating-mixer and an integrated inductor is used. Both prototypes have area and power consumption below state of the art receivers with similar level of performance. The receiver prototypes are based on a low-IF architecture and include also a base band variable gain complex filter for channel selection and image rejection.**

***Index Terms*—Current reuse, LC-tank oscillator, low power, low voltage, low-IF architecture, RF receiver, self-oscillating mixer (SOM), ZigBee receiver.**

## I. Introduction

THE cost and the power consumption of mobile handsets have influenced the evolution of wireless networks architectures and with it their diffusion. In the first cellular systems (TACS, AMPS [1]) the use of large cells allowed to cover wide areas (rural and metropolitan districts) with a minimum number of base-stations, sacrificing the amount of coexisting clients in favor of a less-expensive infrastructure. In particular each cell was formed by a central base-station which provided the connectivity between all the mobile terminals (star-network architecture). At the beginning of the 90s, new research in the field of wireless communications produced low-cost mobile terminals, raising the number of potential users. For this reason the cellular infrastructure was redesigned increasing the cell density around metropolitan areas, leading to the introduction of the GSM [2] and successively the UMTS [3] systems. The result of this evolution was a much more powerful and versatile system. Nevertheless the star-mesh was preserved as the base of a system formed by low-cost mobile handsets and expensive base-stations able to manage a global communication network.

In order to reduce the cost of wireless technology, WLAN/WPAN systems were proposed for data sharing amongst a small group of users. In this case, the easier management of the clients allowed to discard the star-mesh architecture in favor of a more flexible peer-to-peer configuration. Within this evolving scenario, the ZigBee [4] and the other wireless sensor networks (WSN) standards represent an additional step towards the creation of an even more flexible system able to reshape itself dynamically. These systems do not require any base-station, since they are formed by autonomous short-range wireless nodes. All these nodes monitor and control the environment defining the working area by their spatial distribution. Since the high density of units makes the system more flexible and relaxes the sensitivity of the single receiver, in ZigBee network performance is exchanged with the possibility of having long-lasting and cheap devices [5]–[15]. Unfortunately, high efficiency and low-cost tend to trade-off with each other making it difficult to achieve both of them simultaneously. As an example the use of resonant loads minimizes power consumption, while an inductor-free approach reduces the cost by saving die-area.

Two ZigBee receivers based on the LMV cell [16] that can give both power and area saving through current and circuit reuse, are reported in this paper. In the standard LMV cell quadrature down-conversion is performed by cross-coupling two identical cells. In terms of power consumption it can be shown that the figure of merit (FoM) of two quadrature oscillators can be the same as that of a single oscillator [17]. However, the use of two *LC* tanks in the coupled oscillators gives a significant penalty in term of size. To overcome this limitation an alternative receiver architecture that uses a single LO together with an LNA with I and Q outputs is introduced (Fig. 1). Its main drawback is the extra noise associated with the circuits that performs the quadrature. However, in the case of sensor networks like ZigBee, the noise figure requirements are not particularly challenging, making it feasible to perform quadrature in the RF signal path [7].

This paper presents two implementations of the architecture of Fig. 2, which include, in addition to the front-end just described, the base-band portion. They differ only in the practical way in which the RF signal quadrature is generated. In the first implementation the quadrature circuits are biased reusing the current of two LMV cells. In the second implementation, the LNA does not share the bias current with the SOM and the

Manuscript received September 01, 2009; revised October 30, 2009; accepted May 13, 2010. Date of current version August 25, 2010. This paper was approved by Associate Editor Ranjit Gharpurey. This work was supported by the Italian National Program FIRB under Contract RBAP06L4S5.

The authors are with the Microelectronics Laboratory, Department of Electronics, University of Pavia, 27100 Pavia, Italy, (e-mail: antonio.liscidini@unipv.it).

Digital Object Identifier 10.1109/JSSC.2010.2053861

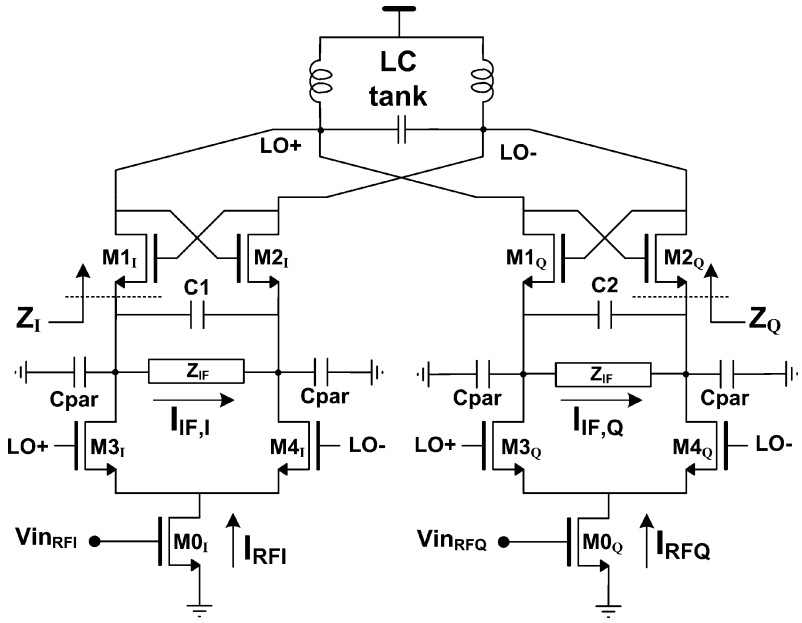


Fig. 1. Single *LC* tank quadrature LMV cell.

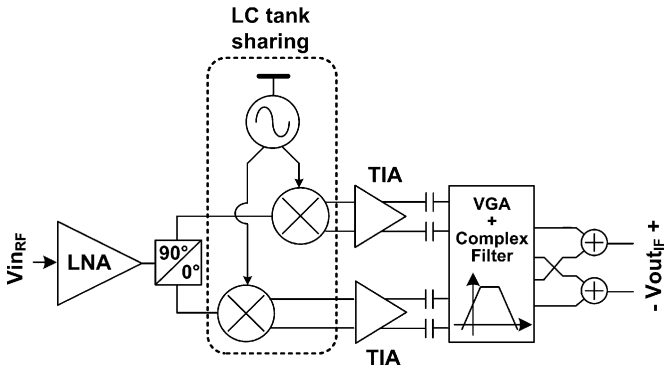


Fig. 2. Proposed RF-front-end and base-band receiver architecture.

quadrature is generated by a RC-CR passive network [18], [19]. The choice between the two implementations is related to the noise target and to the quality factor of the available inductors. To understand the pros and cons of the two alternative architectures, the characteristics of the single coil LMV cell will be analyzed first.

The paper is organized as follows: in Section II the LMV cell is introduced, together with an optimization technique to reduce the losses that affect the conversion gain. In Section III, the LMV cell is modified to produce a single coil quadrature front-end receiver. Successively, new techniques to minimize the potential negative effects of the *LC* tank sharing are introduced. In Section IV the connection between the LNA and the self oscillating mixer (SOM) is discussed, leading to different quadrature generation and LNA input matching circuits. The complete receiver architectures are presented in Section V, together with the base-band design details. Finally, a set of experimental measurements performed on two 90 nm integrated receivers prototypes are reported and some conclusions are drawn in Section VI.

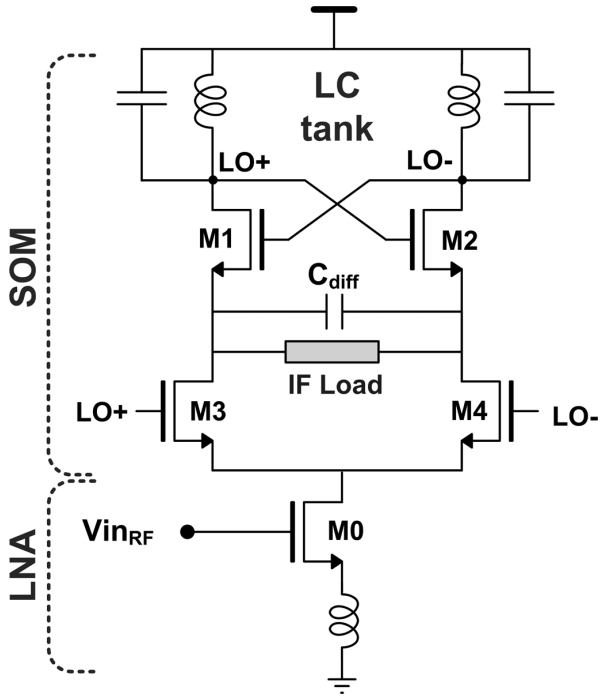


Fig. 3. LMV cell (bias not shown).

## II. LMV Cell: Improvement Through Differential *LC* Tank

The core of the two receivers presented here is the LMV cell (Fig. 3), whose working principle, together with the analysis of its conversion gain, are given in [16]. In this section a conversion gain improvement technique based on the use of a differential *LC* tank is introduced.

The LMV cell performs RF amplification, mixing and LO generation in a single circuit. This allows to share bias current

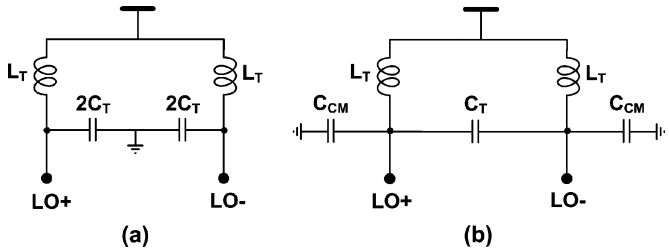


Fig. 4. (a) Common mode and (b) differential *LC* tank.

and devices among all the blocks of the RF front-end. More explicitly, transistor M0 in Fig. 3 sets the voltage-controlled-oscillator (VCO) bias current, while it acts as an LNA at radio frequency (RF). Moreover M1 and M2 (with M3-M4) perform the mixing task while contributing, together with capacitor $\mathrm{C_{diff}}$, to the VCO operation (M1 to M4 built up a self oscillating mixer [18], [19]).

Although the merging of several building blocks is generally associated with a reduced flexibility, the LMV cell can be easily inserted in a conventional PLL for quadrature LO generation [16]. Furthermore, the cell offers the possibility to sense the down-converted current on a virtual ground or the down-converted voltage on a high impedance load. As shown in [16] the current mode approach is less sensitive to parasites, both at low and high frequency, and therefore it is generally preferred to the voltage mode one. The conversion gain (CG) of the current mode LMV cell is defined as the ratio between the IF output differential current and the RF input current. Assuming an ideal load at the output (zero differential impedance), CG depends on the current partition between the RF common mode impedance at the output nodes (dominated by the parasitic capacitors $\mathrm{C_{par}}$) and that at the sources of M1 and M2 (dominated by the *LC* tank common mode impedance $\mathrm{Z_{tankCM}}/2$) [16] and can be expressed as follows:

$$CG = \frac{1}{\pi}\frac{2 + j\omega_{\mathrm{RF}} C_{\mathrm{par}} Z_{\mathrm{tank}} CM(\omega_{\mathrm{RF}})}{1 + j\omega_{\mathrm{RF}} C_{\mathrm{par}} Z_{\mathrm{tank}} CM(\omega_{\mathrm{RF}})}. \tag{1}$$

Additional losses with respect to the ideal gain value of $2/\pi$ occur when $\mathrm{Z_{tankCM}}$ is high. In [16] the *LC* tank topology shown in Fig. 4(a) was used. This topology will be indicated hereafter as common mode *LC* tank since it resonates for both common mode and differential signals. In this case $\mathrm{Z_{tankCM}}$ at the oscillator frequency ($\omega_{LO}$) is equal to $\omega_{\mathrm{LO}}\mathrm{L}_T\mathrm{Q}_T$, resulting in a conversion gain ($\mathrm{CG_{CMtank}}$) given by

$$CG_{\mathrm{CMtank}} = \frac{1}{\pi}\frac{2 + j\omega_{\mathrm{LO}} C_{\mathrm{par}} \omega_{\mathrm{LO}} L_T Q_T}{1 + j\omega_{\mathrm{LO}} C_{\mathrm{par}} \omega_{\mathrm{LO}} L_T Q_T}. \tag{2}$$

Since high $\mathrm{Q}_T$ reduces the SOM conversion gain while improving the oscillator FoM, a trade-off is introduced. This issue can be overcome using the differential *LC* tank topology of figure Fig. 4(b), that presents a lower common mode impedance at the LO frequency the proper differential impedance (to set the oscillation frequency) and a DC path for the bias of the SOM. Since a purely differential *LC* tank can be realized only ideally, capacitors $\mathrm{C_{CM}}$ are added in Fig. 4(b) to represent the unavoidable parasites at the oscillator outputs. The differential *LC* tank introduces an extra degree of freedom, since the common mode and differential impedances resonate at different frequencies. In particular the common mode resonance frequency, which depends only on $\mathrm{C_{CM}}$, is higher than the differential one. The common mode impedance at $\omega_{\mathrm{RF}} = \omega_{\mathrm{LO}}$ can be expressed as follows:

$$Z_{\mathrm{tankCM}}(\omega_{\mathrm{LO}}) = \frac{\omega_{\mathrm{LO}} L_T \left(j + \frac{1}{Q_T}\right) \frac{1}{j\omega_{\mathrm{LO}} C_{\mathrm{CM}}}}{\omega_{\mathrm{LO}} L_T \left(j + \frac{1}{Q_T}\right) + \frac{1}{j\omega_{\mathrm{LO}} C_{\mathrm{CM}}}}. \tag{3}$$

Inserting (3) in (1), the down-conversion gain of the LMV cell with a differential *LC* tank ($\mathrm{CG_{DIFFtank}}$) becomes

$$\begin{aligned} CG_{\mathrm{DIFFtank}} &= \frac{1}{\pi}\frac{2 + j\omega_{\mathrm{LO}} C_{\mathrm{CM}} \omega_{\mathrm{LO}} L_T \left(j + \frac{1}{Q_T}\right)}{1 + j\omega_{\mathrm{LO}}(C_{\mathrm{par}} + C_{\mathrm{CM}})\omega_{\mathrm{LO}} L_T \left(j + \frac{1}{Q_T}\right)} \\ &\cong \frac{1}{\pi}\frac{2 + j\omega_{\mathrm{LO}} C_{\mathrm{CM}} (j\omega_{\mathrm{LO}} L_T)}{1 + j\omega_{\mathrm{LO}}(C_{\mathrm{par}} + C_{\mathrm{CM}})(j\omega_{\mathrm{LO}} L_T)} \end{aligned} \tag{4}$$

where the approximation is valid for $\mathrm{Q}_T$ higher than 10.

The theoretical and simulated LMV cell conversion gain Vs. $\mathrm{C_{par}}$ and $\mathrm{Q}_T$ are reported in Fig. 5 for both *LC* tank topologies. From (2) and (4), regardless of the *LC* tank used, the conversion gain is equal to $2/\pi$ when no parasitic capacitors are present at the IF output, while it tends to $1/\pi$ when $\mathrm{C_{par}}$ tends to infinity. As shown in Fig. 5(a), for intermediate values of $\mathrm{C_{par}}$, the differential *LC* tank gives lower losses compared to the common mode one, producing a conversion gain that can become even higher than $2/\pi$ . This effect is strictly related to $\mathrm{Z_{tankCM}}$ which resonates with $\mathrm{C_{par}}$ producing the same current amplification that occurs in shunt *LC* networks [20]. Referring to Fig. 5(b) the inductor quality factor $\mathrm{Q}_T$ has negligible effect on the gain for a differential *LC* tank, while for a common mode *LC* tank the gain varies from a maximum of $2/\pi$ to a minimum of $1/\pi$ as $\mathrm{Q}_T$ increases.

This analysis proves that a differential *LC* tank makes the mixer gain less sensitive to parasitic and independent from the inductor $\mathrm{Q}_T$, allowing the use of high quality factor inductors to reduce the VCO power consumption without degrading the gain.

## III. Single Coil Quadrature LMV Cell

The generation of I and Q signals can be easily performed using a single *LC* tank. A possible strategy is to use an oscillator at twice the frequency of interest and generate the I and Q LO's through frequency dividers. Unfortunately this solution cannot be used in the LMV cell where the switching pairs are driven by signals at the same frequency as the LO. The proposed single coil quadrature LMV cell, is reported in Fig. 1 where the I and Q path use the same LO but quadrature is performed in the RF path. In addition to the extra cost of the RF quadrature circuits, sharing the *LC* tank introduces additional mechanisms for amplitude/phase mismatches in the I and Q conversion gains. This can be understood considering that losses in the I and Q paths depend on the current partition between the impedances $\mathrm{Z_I}$ and $\mathrm{Z}_Q$ respectively, and the parasitic capacitors at the IF

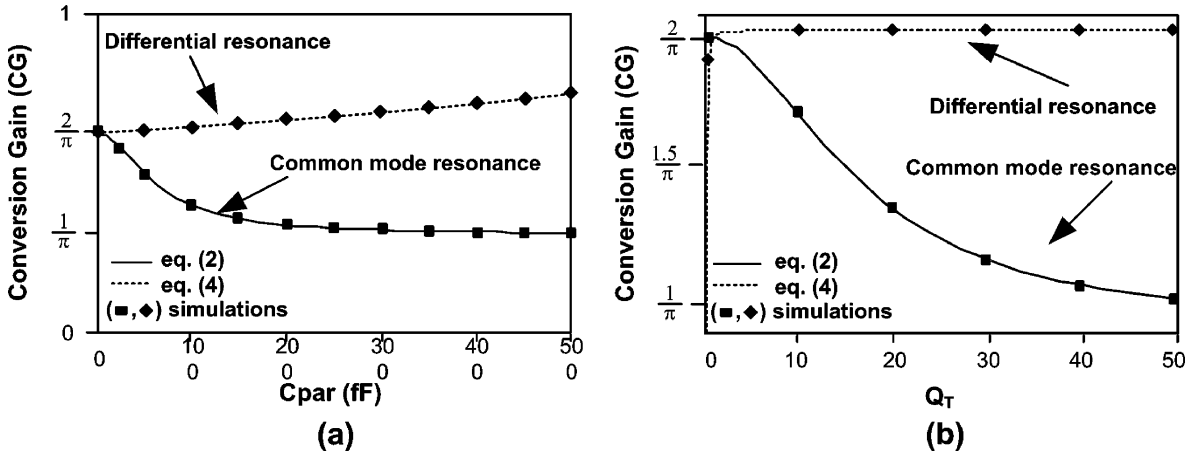


Fig. 5. (a) SOM conversion gain as function of $C_{par}$ and (b) as function of $Q_T$ ($f_0 = 2.45$ GHz, $L_T = 2$ nH, $C_{par} = 100$ fF).

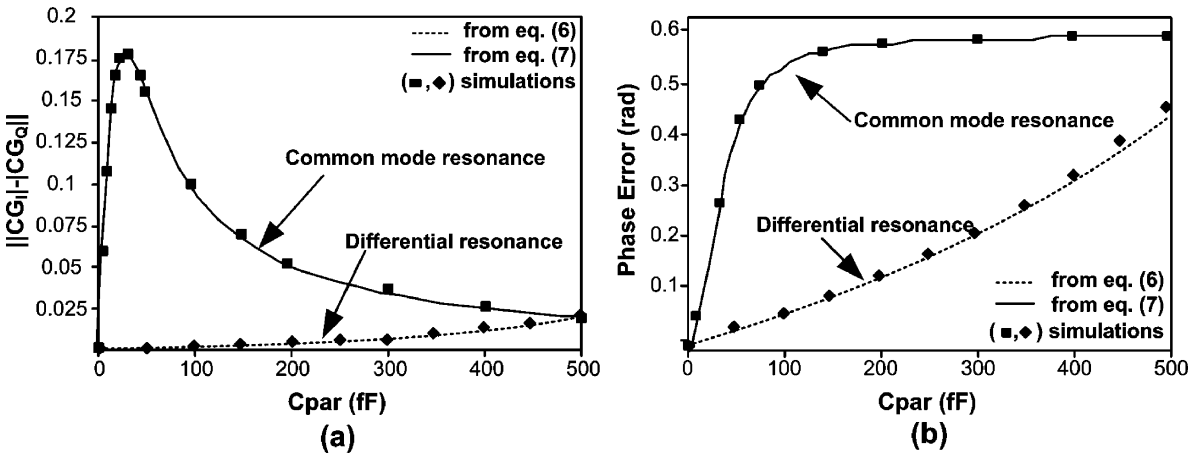


Fig. 6. (a) Quadrature SOMs amplitude mismatch and (b) phase error as function of $C_{par}$ ($f_0 = 2.45$ GHz, $L_T = 2$ nH, $C_{CM} = 300$ fF).

nodes (Fig. 1). The expressions for $Z_I$ and $Z_Q$ were derived in [21], and are reported below:

$$\begin{cases} Z_I(\omega_{RF}) = \frac{Z_{tankCM}(\omega_{RF})}{2}(1-j) \\ Z_Q(\omega_{RF}) = \frac{Z_{tankCM}(\omega_{RF})}{2}(1+j) \end{cases}. \quad (5)$$

Since these impedances are complex conjugates, they produce different (in both amplitude and phase) current partitions in the I and Q paths. Starting from (5), the current losses can be calculated as shown in [16] and from that, the expressions for the I and Q paths conversion gain can be derived. For the case of a differential resonator the two conversion gains have the following expressions:

$$\begin{cases} CG_{I-DIFFtank} = \frac{1}{\pi}\frac{2(1-\omega_{LO}^2 C_{CM} L_T)-(3-j)\omega_{LO}^2 C_{par} L_T}{1-\omega_{LO}^2 C_{CM} L_T - 2\omega_{LO}^2 C_{par} L_T} \\ CG_{Q-DIFFtank} = \frac{1}{\pi}\frac{2(-1+\omega_{LO}^2 C_{CM} L_T)+(3+j)\omega_{LO}^2 C_{par} L_T}{-1+\omega_{LO}^2 C_{CM} L_T + 2\omega_{LO}^2 C_{par} L_T} \end{cases} \quad (6)$$

while for the case of a common mode resonator , their expressions are the following:

$$\begin{cases} CG_{I-CMtank} = \frac{1}{\pi}\frac{2+\omega_{LO}^2 C_{par} L_T Q_T (3j+1)}{1+2j\omega_{LO}^2 C_{par} L_T Q_T} \\ CG_{Q-CMtank} = \frac{1}{\pi}\frac{2+\omega_{LO}^2 C_{par} L_T Q_T (3j-1)}{1+2j\omega_{LO}^2 C_{par} L_T Q_T} \end{cases}. \quad (7)$$

Fig. 6 shows the theoretical and simulated conversion gain difference between the I and Q path (for both amplitude and phase) versus the value of the parasitic capacitance $C_{par}$ at the IF output node. The plot is obtained assuming a fairly conservative value of 300 fF for $C_{CM}$. The figure shows that the total error is smaller for the differential *LC* tank compared to the common mode implementation in a range of $C_{par}$ values which exceed what can be found in a typical design. In particular, for a differential resonator, both phase and amplitude errors remain acceptable for ZigBee applications if $C_{par}$ stays below 300 fF, while this is not the case for the common mode resonator. From these considerations, it follows that in the quadrature front-end a differential *LC* tank topology should be used.

## IV. Quadrature Generation and LNA Input Matching

The proposed single coil quadrature LMV cell has to be driven with both in-phase and quadrature RF signals which should be generated at minimum cost in terms of power consumption. Different quadrature generation technique and strategies to obtain input matching can be chosen, depending on the bias sharing between the LNA and the SOM. For example, the low-noise-amplifier can be stacked with the SOM, or it can be fed by an independent current source.

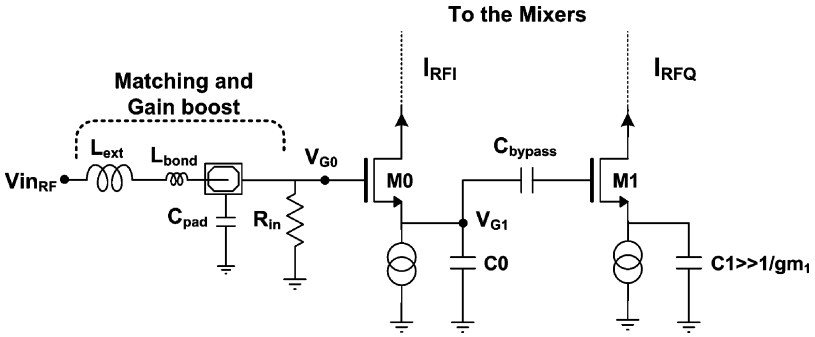


Fig. 7. LNA input matching and quadrature generation through capacitive degeneration (used in prototype I).

When a low $Q_T$ (less than 20) *LC* tank is used, the optimal bias current of the VCO is comparable with that of the LNA, and stacking these blocks can implement input matching, amplification and down-conversion without requiring any extra power consumption in addition to the one used by the SOM. In this case RF signals quadrature can be obtained through capacitive degeneration [17] as detailed below. Such a choice, however, does not exploit the noise advantages of an inductively degenerated LNA.

On the contrary, an inductively degenerated LNA can be used if the LNA is not stacked with the SOM. In this case the RF signal quadrature has to be performed at the LNA output through an RC-CR load as detailed below. This solution is particularly suitable when a high $Q_T$ inductor (e.g., a bondwire) is used in the SOM. In fact, in such a case a small current can be used both in the SOM to achieve the desired LO amplitude and in the emitter degenerated LNA to obtain the target noise figure. This approach is also less costly, since it eliminates expensive integrated coils.

### A. Quadrature by Capacitive Degeneration

When low $Q_T$ integrated coils are used, the 90° phase shift in the RF signal is done as shown in Fig. 7 [17]. The source of transistor M0 is degenerated with a capacitor C0 and its drain current is sent to the I input of the mixer. At the same time the voltage at the source of M0 is connected through the bypass capacitor ($C_{bypass}$) to the gate of transistor M1 that behaves as a common source stage thanks to the big capacitance C1 at its source. In this way, the drain current of M1 (that goes to the I input of the mixer) is in quadrature with the drain current of M0 (which goes to the Q input of the mixer). The phase relationship of the two LNA output currents $I_{RFI}$ and $I_{RFQ}$ can be obtained from the following expressions:

$$\begin{cases} I_{\mathrm{RFI}} = \frac{j\omega C0}{1+j\omega\frac{C0}{gm_0}} V_{G0} \\ I_{\mathrm{RFQ}} = \frac{gm_0}{j\omega C0} I_{\mathrm{RFI}} \end{cases}. \tag{8}$$

From (8), the 90° phase shift is guaranteed in a wide frequency range while the amplitude matching is only obtained around $\omega_0$ setting $C0 = gm/\omega_0$. Nonetheless the amplitude error for $\omega \neq \omega_0$ remains sufficiently low in the frequency range of interest to satisfy with good margin the specifications of the ZigBee standard.

While inductive degeneration synthesizes a positive resistance, capacitive degeneration produces an input impedance whose real part is negative and can be expressed as:

$$Re[Zn] = -\frac{gm_0}{\omega^2 C_{gsM0} C0}. \tag{9}$$

Input matching is obtained adding an integrated resistor $R_{in}$ in parallel with the input and an L-match network (Fig. 7). The value of $R_{in}$ must be chosen to provide input matching in the presence of the unwanted negative resistance that appears in parallel with it. Since capacitive degeneration creates a negative resistance, stability needs to be carefully considered. Stability is guaranteed if the quality factor of the network formed by the pad capacitance and the resistance $R_{in}$ is greater than the absolute value of the quality factor and of the network formed by transistor M0 and capacitance C0.

Although the use of a passive termination tends to increase the noise figure, this effect is mitigated by the presence of a resonant circuit at the input which boosts the LNA transconductance providing voltage gain at the gate of M0. Finally, inductor $L_{ext}$ in Fig. 7, together with the pad capacitance, forms a narrowband input filter, which prevents harmonic locking phenomena in the presence of large blockers at the double of SOM oscillation frequency [17].

### B. Quadrature Through RC-CR Load

When high-Q inductors are used in the *LC* tank, the LNA is biased with a separate current and an RC-CR load at the LNA output generates quadrature in the RF path [21], as shown in Fig. 9. The load network has to synthesize a zero and a pole at $\omega_0$, while trading off between noise and area. As in the previous case, even if exact I/Q amplitude matching is obtained only at $\omega_0$, the mismatch remains sufficiently low in the entire frequency range set by the standard.

An inductively degenerated LNA has the best power/noise performance although the use of integrated inductors increases the die area. To minimize costs, the degeneration inductance of the LNA can be formed with a bond-wire [21]. Since there is some concern about the reproducibility of bond-wire inductors, to compensate the variations of $L_{bond1,2}$, an external inductor ($L_{ext}$) is added in series with $L_{bond1}$. $L_{ext}$ compensates the effect of bond-wires variations making it possible to set the proper resonance frequency for the matching network. This technique

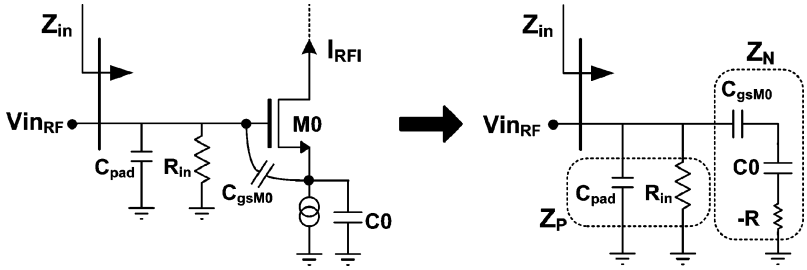


Fig. 8. Impedance synthesized by a capacitive degeneration.

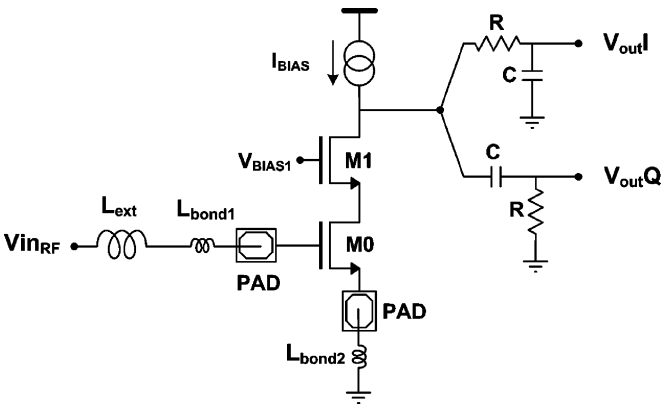


Fig. 9. LNA Input matching and quadrature generation through RC-CR load (used in prototype II).

allows also to keep constant the quality factor of the input network which controls the impedance matching. As in the previous case, the matching network creates a narrowband filter at the input that has the added benefit of avoiding any injection-locking phenomena [17].

## V. Receiver Architecture and Base Band Design

Fully integrated receivers usually perform a down-conversion of the RF signal at a low intermediate frequency (low-IF architecture) or at DC (direct-conversion architecture)[23]. The direct-conversion receiver does not suffer from the image problem, but it is sensitive to DC-offsets (including the one introduced by the second order non linearity of the mixer), and to the flicker noise of CMOS transistors. The schematic of the receiver chain is shown in Fig. 2. The down converted signal current produced by the SOM is sensed at IF through a virtual ground implemented with a trans-impedance amplifiers (TIAs). The output signals of the I and Q TIAs are then combined through a complex third order filter that performs image rejection and channel selection.

### A. Virtual Ground Design Details

The trans-impedance amplifier is based on a gain boosted cascode configuration (Fig. 10(a)). This topology makes it possible to synthesize a low impedance $\mathrm{Z_{indiff}}$ over a large bandwidth. At low frequency the input impedance is:

$$Z_{\mathrm{indiff}} \cong \frac{2}{A_0 \cdot gm_{\mathrm{casc}}} \tag{10}$$

where $\mathrm{A_0}$ is the DC gain of the core amplifier. To obtain a good virtual ground the product $\mathrm{A_0 gm_{casc}}$ should be maximized over frequency. For a given bias current, $\mathrm{gm_{casc}}$ can be increased by choosing a larger aspect ratio for the two transistors $\mathrm{M_{casc}}$, but at the cost of a larger parasitic capacitors at the IF output nodes, which affects the SOM down-conversion gain and amplitude/phase errors, as explained before. A higher transconductance of transistors $\mathrm{M_{casc}}$ can be obtained also increasing their bias current, at the cost of a greater power dissipation. Since the $\mathrm{gm_{casc}}$ maximization introduces some drawbacks, $\mathrm{Z_{indiff}}$ is reduced maximizing the amplifier gain $\mathrm{A_0}$ over a large bandwidth compared with the ZigBee standard requirement (3 MHz). This is obtained using a folded cascode core, which also minimizes the amplifier capacitive load, made up of the series of $\mathrm{C_{gsIN}}$ and $\mathrm{C_{ddBIAS}}$ (Fig. 10(b)). The amplifier has a simulated gain equal to 31 dB over a bandwidth of about 10 MHz, producing a differential impedance of about 20 $\Omega$ over a 10 MHz frequency band with a total current consumption of about 60 $\mu$A. Notice that providing low impedance over a large bandwidth for the virtual ground not only limits current losses but also results in high linearity in the presence of large interferers.

### B. Channel Selection Filter Design Details

The base band filter performs channel selection and image rejection. For the ZigBee standard, a 3rd order complex filter can satisfy the requirements with good margin [7]. The complex filter can be obtained from a 3rd order Butterworth real filter, where the poles are shifted along the imaginary axis [24] thereby shifting by the same amount the filter transfer function (Fig. 11).

Since for the ZigBee standard linearity is relaxed while power consumption is severely constrained, a $\mathrm{gm\text{-}C}$ filter topology was chosen [25], [26] . To make the design as simple and as modular as possible, the 3rd order filter is implemented as the cascade of three single complex poles. As shown in Fig. 12, to synthesize a single pole, two $\mathrm{gm\text{-}C}$ stages with real transfer function are transformed into a complex one by adding an imaginary term obtained cross-connecting the I and Q transconductances $\mathrm{gm_{IM}}$. The location of the pole in the complex plane can be expressed as:

$$\omega_{comp} = \frac{gm_{RE}}{2C} + j\frac{gm_{\mathrm{IM}}}{2C}. \tag{11}$$

The real part of the synthesized poles determines the filter bandwidth, while the imaginary part sets the filter central frequency. The gain and the pole location of each stage can be calibrated changing the MOS transconductance acting on the

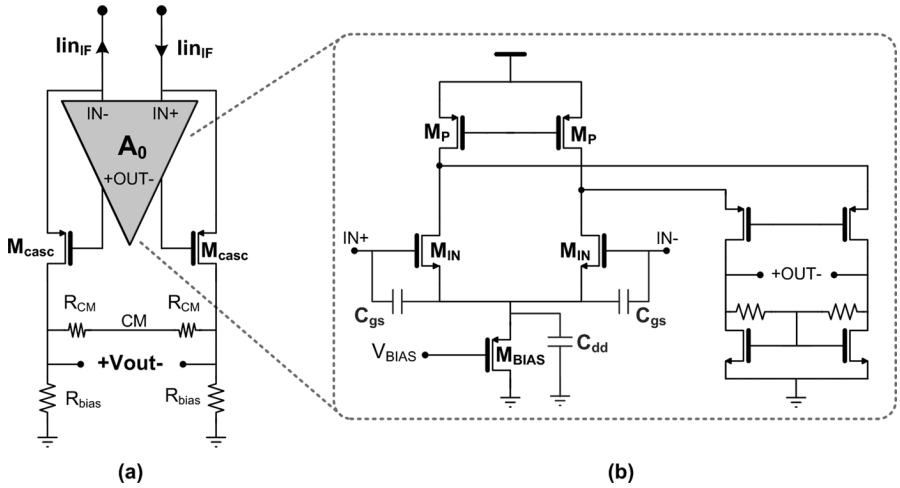


Fig. 10. Virtual ground design details.

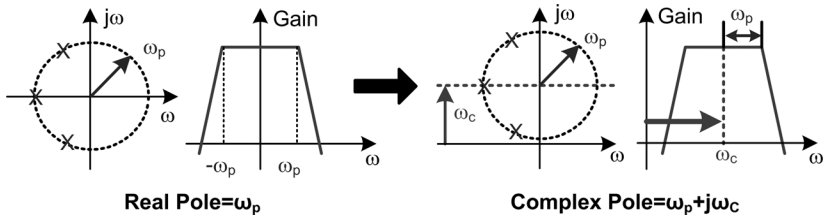


Fig. 11. Poles and transfer function in a real and complex filter.

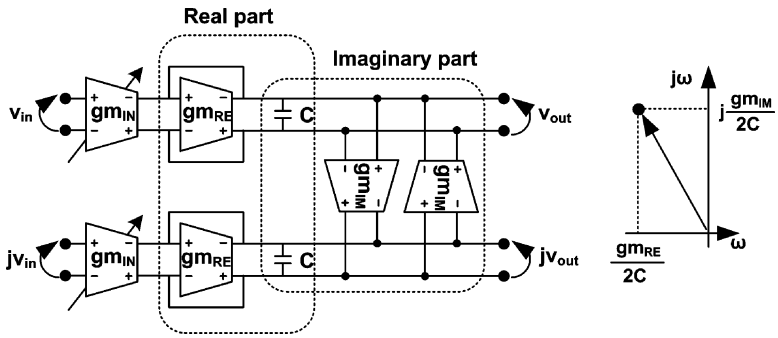


Fig. 12. Block diagram of the $\mathrm{gm}$-C complex filter stage (one pole synthesized).

bias current $\mathrm{I_{BIAS}}$. Notice that while the central frequency is well defined the filter bandwidth depends also on the $\mathrm{g_{ds}}$ of the other transconductance stages. Therefore, to reduce this spurious effect, each transconductor is implemented with a cascode topology, as shown in Fig. 13.

## VI. Measurements Results

The two receivers have been placed on the same chip and integrated using a 90 nm CMOS technology. The two receivers use the same base-band and are different only in the RF section (VCO with bond-wires or integrated inductor). Pads are ESD protected and for ground and supply multiple pads with multiple bond-wires are used. The micrograph of the two prototypes is shown in Fig. 14. The RF front-end and the base band section have been marked. In both prototypes the oscillator is free-running, even if the proposed receivers need to have a PLL to set the channel frequency. However, as demonstrated in a previous work, the use of a PLL does not represent a challenge for this structure [16].

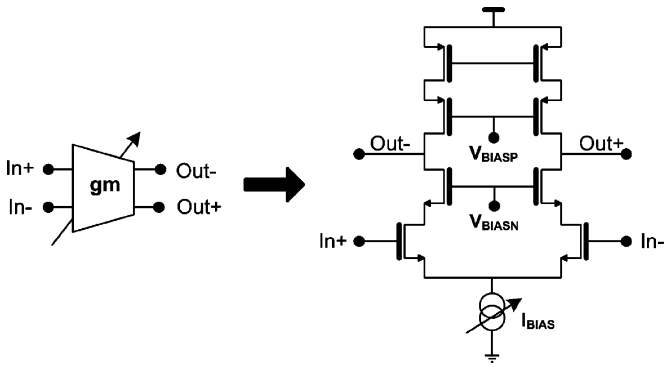


Fig. 13. Double-cascode transconductor used in the design of the $\mathrm{gm}$-C filter.

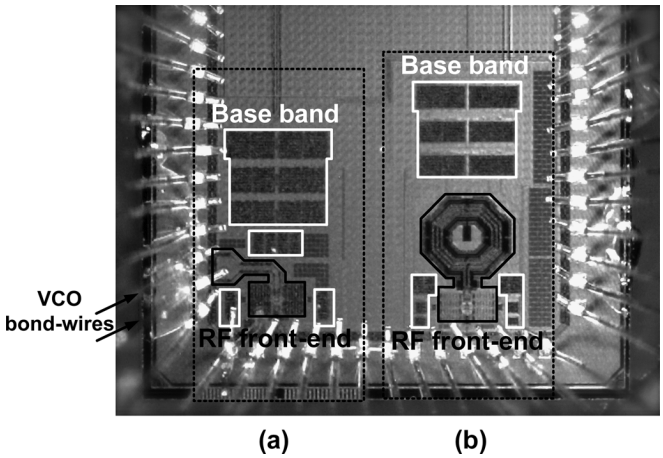


Fig. 14. (a) Free-coil and (b) integrated coil prototype micrographs.

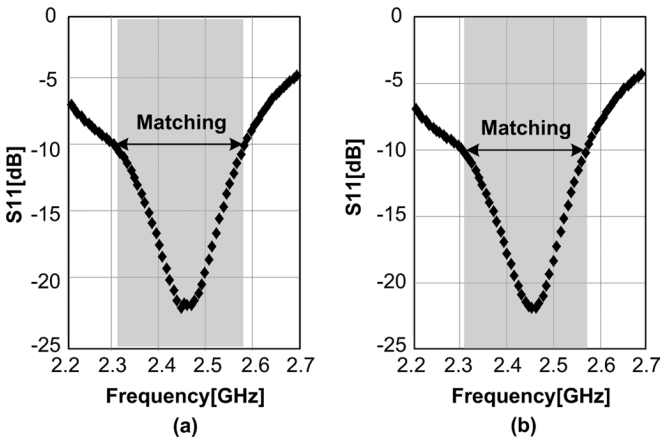


Fig. 15. Measured S11 of the (a) free-coil and (b) single integrated coil prototype ($f_{LO} = 2.45$ GHz).

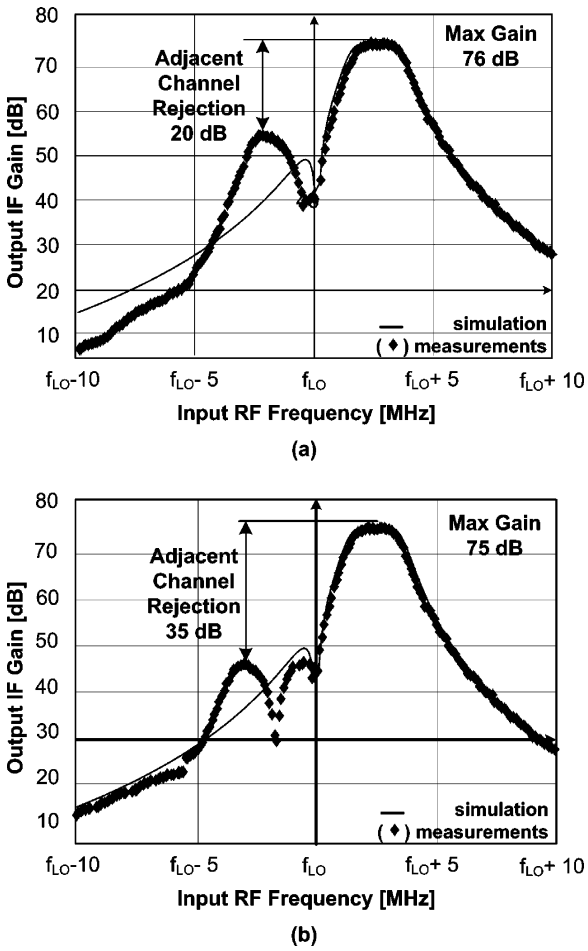


Fig. 16. Measured IF gain profile of the (a) free-coil and (b) single integrated coil prototype.

The coil-free receiver has aluminum bond-wire inductors, with a diameter of less than 30 $\mu$m and a length around 1.5 mm. Their estimated quality factor is around 35. The resulting active die area is 0.23 mm$^2$, while the area of the version that uses an integrated inductor increases to 0.35 mm$^2$. The area difference between the two versions becomes much more significant if only the RF portion of the die is considered. In fact, the base-band portion, common to the two implementations, has an area of about 0.2 mm$^2$, i.e., almost 90% of the total coil free version. This is contrary to what typically occurs in integrated transceivers, where the limiting factor for die area minimization is the RF front-end. For the RF front-end, the single coil prototype requires about 0.15 mm$^2$ and the coil-free one only 0.03 mm$^2$.

The die was bonded on a dedicated RF board with gold plated micro-strip interconnect on an FR4 substrate. Properly sized 50 $\Omega$ strip lines carry the input signal from the SMA connectors to the die. The input reflection coefficient measurements are reported in Fig. 15. Both termination techniques used result in a good input matching at the ZigBee frequency (S11 always better than $-18$ dB). The frequency response of the receiver at the channel selection filter output is reported in Fig. 16. The maximum in band gain exceeds 75 dB (from 1 to 3 MHz) in both prototypes, while the image rejection, obtained without any calibration, is quite different in the two cases (20 dB versus 30 dB). Nonetheless in both cases the achieved value ensures a safe margin form the target spec of 4 dB. The reduced image rejection value for the coil free case is due to an incorrect estimation of the parasitic capacitance of the RC-CR network, which introduces an error in the desired 90° phase shift between the I and Q signals. On the other hand, the error associated with the shared coil I and Q SOMs was made almost negligible through the use of a differential resonant tank as shown by the integrated inductor version.

Other measurements on the coil-free prototype show a noise figure integrated over the IF band (from 1 MHz to 3 MHz), of about 10 dB, and an in band IIP3 of $-13$ dBm. The IIP3 test is performed using two tones respectively at 10 MHz and 22 MHz from the carrier. The measured VCO phase noise at 3.5 MHz from the carrier (as defined by the ZigBee standard [4]) is about $-124$ dBc/Hz. Similar performance is displayed by the integrated coil prototype, which has an average noise figure between 1 MHz and 3 MHz of 9 dB, an in band IIP3 of $-12.5$ dBm and a VCO phase noise at 3.5 MHz of $-116$ dBc/Hz. Notice that the larger NF for the coil-free prototype is due to the error in the quadrature generating RC-CR network (as explained before). The 8 dB difference in phase noise between the two versions

TABLE I
STATE OF THE ART OF ZIGBEE RECEIVERS

| | [5] | [6] | [7] | [8]* | [9]** | This work prototype I | This work prototype II |
|---|---|---|---|---|---|---|---|
| Gain [dB] | --- | --- | --- | --- | 33 | 75 | 76 |
| NF [dB] | 24.7 | 7.3 | 5.7 | 7 | 7.5 | 9 | 10 |
| IIP3 [dBm] | -4.5 | -8 | -16 | -7.5 | -10 | -12.5 | -13 |
| SFDR [dB] | 50.3 | 59.5 | 55.3 | --- | 58.3 | 55.5 | 54.4 |
| PN @ 3.5 MHz [dBc/Hz] | --- | --- | --- | -116.9 | --- | -116 | -124 |
| Power diss [mW] | 15 | 6.3 | 17 | 1.45 | 5.4 | 3.6 | 3.6 |
| Integrated inductors | 6 | 2 | 4 | 3 | 2 | 1 | 0 |
| area [$mm^2$] | 2.1 | 2.075 | 0.8 | 1.8 | 0.23 | 0.35 | 0.23 |
| Vdd [V] | 1.8 | 1.8 | 1.8 | 0.4 | 1.35 | 1.2 | 1.2 |
| Technology [$\mu$m] | 0.18 | 0.18 | 0.18 | 0.13 | 0.09 | 0.09 | 0.09 |

*Proprietary wireless- sensors- networks standard

** Voltage-controlled-oscillator not included

derives from the different quality factor of the bond-wire tank versus the integrated inductor tank.

Both prototypes dissipate 3.6 mW (3 mA from a 1.2 V supply). The total drawn current of 3 mA, is divided in 2 mA for the RF blocks and 1 mA for the TIAs and the baseband filter. In the coil free prototype the supply voltage can be lowered down to 1 V still maintaining proper operation, since the SOM and the LNA are not stacked.

In Table I the measurement results for the two prototypes are reported and compared to the state of the art for complete ZigBee receivers. Even if some of the works reported in Table I contains also a PLL, the comparison is realized considering only size and power consumption of LNA, Mixer and VCO. The table includes also the spurious free dynamic range (SFDR) of the various implementations which accounts at the same time for the noise figure (or sensitivity) and the linearity (IIP3) according to the following definition [27]:

$$\mathrm{SFDR} = \frac{2(\mathrm{IIP3} - \mathrm{F})}{3} - \mathrm{SNR}_{\min} \tag{12}$$

where F is the noise floor integrated over the band of interest and $\mathrm{SNR}_{\min}$ is the minimum signal-to-noise ratio required by the application (in this case it is assumed to be 4 dB, as reported in [7]). Both prototypes presented show a SFDR in line with the state-of-the-art, but require less than half of the die area of previous implementations and use much less power consumption.

## ACKNOWLEDGMENT

The authors want to thank A. Baschirotto for fruitful discussion, M. Galli for the support in the setup of test equipment, Marvell for providing technology access, and S. Shia (TSMC) for his support.

## REFERENCES

[1] M. P. Metroka, "An introduction to narrowband AMPS," in *Proc. GLOBECOM*, Dec. 1991, vol. 2, pp. 1463–1468.

[2] M. Rahnema, "Overview of the GSM system and protocol architecture," *IEEE Commun. Mag.*, vol. 31, no. 4, pp. 92–100, Apr. 1993.

[3] A. Samukic, "Universal mobile telecommunications system: Development of standards for the third generation," *IEEE Trans. Veh. Technol.*, vol. 47, pp. 1099–1104, Nov. 1998.

[4] *Low Rate Personal Area Network*, IEEE Standard 802.15.4-2003, Oct. 2004.

[5] P. Choi *et al.*, "An experimental coin-size radio for extremely low-power WPAN (IEEE 802.15.4) applications at 2.4 GHz," *IEEE J. Solid-State Circuits*, vol. 38, no. 12, pp. 2258–2268, Dec. 2003.

[6] T. K. Nguyen *et al.*, "A low-power RF direct-conversion receiver/transmitter for 2.4-GHz-band IEEE 802.15.4 standard in 0.18-$\mu$m CMOS technology," *IEEE Trans. Microw. Theory Tech.*, vol. 54, pp. 4062–4071, Dec. 2006.

[7] W. Kluge *et al.*, "A fully integrated 2.4 GHz IEEE 802.15.4 compliant transceiver for ZigBee applications," *IEEE J. Solid-State Circuits*, vol. 41, no. 12, pp. 2767–2775, Dec. 2006.

[8] B. W. Cook *et al.*, "Low-power, 2.4-GHz transceiver with passive RX front-end and 400-mV supply," *IEEE J. Solid-State Circuits*, vol. 41, no. 12, pp. 2757–2766, Dec. 2006.

[9] M. Camus *et al.*, "A 5.4 mW 0.07 $mm^2$ 2.4 GHz front end receiver in 90 nm CMOS for IEEE 802.15.4 WPAN," *IEEE J. Solid-State Circuits*, vol. 43, no. 6, pp. 1327–1383, Jun. 2008.

[10] A. A. Hafez *et al.*, "Design of a low-power ZigBee receiver front-end for wireless sensors," in *Proc. Int. Conf. Microelectronics*, Dec. 2007, pp. 183–186.

[11] H. M. Seo *et al.*, "A low power fully CMOS integrated RF transceiver IC for wireless sensor networks," *IEEE Trans. VLSI Syst.*, vol. 15, no. 2, pp. 227–231, Feb. 2007.

[12] I. Nam *et al.*, "A 2.4-GHz low-power low-IF receiver and direct-conversion transmitter in 0.18 $\mu$m CMOS for IEEE 802.15.4 WPAN applications," *IEEE Trans. Microw. Theory Tech.*, vol. 55, pp. 682–689, Apr. 2007.

[13] S. Sarhangian, S. M. Atarodi, and M. 2007, "A low-power CMOS low-IF receiver front-end for 2450-MHz band IEEE 802.15.4 ZigBee standard," in *Proc. IEEE Int. Symp. Circuits and Systems (ISCAS 2007)*, May 2007, pp. 433–436.

[14] Y. S. Hwang and H. J. Yoo, "A low power folded RF front-end with merged LNA and mixer for ZigBee/Bluetooth," in *Proc. IEEE Radio and Wireless Symp.*, Jan. 2007, pp. 85–867.

[15] C. Bernier *et al.*, "An ultra low power 130 nm CMOS direct conversion transceiver for IEEE 802.15.4," in *IEEE RFIC Dig. Tech. Papers*, Jun. 2008, pp. 273–276.

[16] A. Liscidini *et al.*, "Single-stage low-power quadrature RF receiver front-end: The LMV cell," *IEEE J. Solid-State Circuits*, vol. 41, no. 12, pp. 2832–2841, Dec. 2006.

[17] A. Liscidini, M. Tedeschi, and R. Castello, "A 2.4 GHz 3.6 mW 0.35 $mm^2$ quadrature front-end RX for ZigBee and WPAN applications," in *IEEE ISSCC Dig. Tech. Papers*, Feb. 2008, pp. 370–371.

[18] J. van der Tang and D. Kasperkovitz, "A 0.9–2.2 GHz monolithic quadrature mixer oscillator for direct-conversion satellite receivers," in *IEEE ISSCC Dig. Tech. Papers*, Feb. 1997, pp. 88–89.

[19] M. Ghanevati and A. S. Daryoush, "A low-power-consuming SOM for wireless communications," *IEEE Trans. Microw. Theory Tech.*, vol. 47, no. 7, pp. 1348–1351, Jul. 2001.

[20] T. H. Lee, *The Design of CMOS Radio-Frequency Integrated Circuits*. Cambridge, U.K.: Cambridge University Press, 1998.
[21] M. Tedeschi, A. Liscidini, and R. Castello, "A 0.23 mm$^2$ free coil ZigBee receiver based on a bond-wire self-oscillating mixer," in *Proc. ESSCIRC*, Sep. 2008, pp. 430–433.
[22] F. Svelto and R. Castello, "A bond-wire inductor-MOS varactor VCO tunable from 1.8 to 2.4 GHz," *IEEE Trans. Microw. Theory Tech.*, vol. 50, no. 1, pp. 403–407, Jan. 2002.
[23] B. Razavi, *RF Microelectronics*. Englewood Cliffs, NJ: Prentice Hall PTR, 1998, pp. 118–148.
[24] J. Crold and M. Steyaert, *CMOS Wireless Transceiver Design*. Boston, MA: Kluwer Academic, 1997.
[25] P. Andreani and S. Mattisson, "On the use of Nauta's transconductor in low-frequency CMOS gm-C bandpass filters," *IEEE J. Solid-State Circuits*, vol. 37, no. 2, pp. 114–124, Feb. 2002.
[26] J. Ko *et al.*, "A 19-mW 2.6-mm$^2$ L1/L2 dual-band CMOS GPS receiver," *IEEE J. Solid-State Circuits*, vol. 40, no. 7, pp. 1414–1425, Jul. 2005.
[27] B. Razavi, *RF Microelectronics*. Englewood Cliffs, NJ: Prentice Hall PTR, 1998, p. 50.

**Marika Tedeschi** (S'06–M'10) received the Laurea (*summa cum laude*) and the Ph.D. in electrical engineering from the University of Pavia, Pavia, Italy, in 2006 and 2010, respectively.

Currently, she is with Marvell Semiconductors as an RFIC design engineer. Her research interests are in the RF and BB design for very low power and multistandard applications.

**Antonio Liscidini** (S'99–M'06) received the Laurea (*summa cum laude*) and the Ph.D. in electrical engineering from the University of Pavia, Pavia, Italy, in 2002 and 2006, respectively.

He was a summer intern at National Semiconductors, Santa Clara, CA, in 2003, studying poly phase filters and CMOS LNA. Currently, he is an Assistant Professor with the University of Pavia. His research interests are in the implementations of analog RF front-end in CMOS and BiCMOS technology, with particular focus on the analysis and design of LNAs for multi-standard applications, ultra low power receivers and digital PLLs. In addition to his academic activities, he has been acting as a consultant for Marvell Semiconductors in the area of integrated circuit design.

Dr. Liscidini received the Best Student Paper Award at IEEE 2005 Symposium on VLSI Circuits. Since December 2007, he has served as an Associate Editor of the IEEE TRANSACTIONS ON CIRCUITS AND SYSTEMS II: EXPRESS BRIEFS. Since 2010, he is a member of the TPC of the European Solid-State Circuits Conference (ESSCIRC).

**Rinaldo Castello** (S'78–M'78–SM'92–F'99) graduated from the University of Genova (*summa cum laude*) in 1977 and received the M.S. and the Ph.D. from the University of California, Berkeley, in 1981 and 1984.

From 1983 to 1985 he was a Visiting Assistant Professor at the University of California, Berkeley. In 1987 he joined the University of Pavia, Pavia, Italy, where he is now a Full Professor. He consulted for ST-Microelectronics, Milan, Italy, up to 2005 and from 1998 to 2005 was the Scientific Director of a joint research center between the University of Pavia and STMicroelectronics. He promoted the establishment of several design centers from multinational IC companies in the Pavia area, including Marvell, for which he has been consulting since 2005.

Dr. Castello has been a member of the TPC of the European Solid-State Circuits Conference (ESSCIRC) since 1987 and of the IEEE International Solid-State Circuits Conference (ISSCC) from 1992 to 2004. He was Technical Chairman of ESSCIRC'91 and General Chairman of ESSCIRC'02, Associate Editor for Europe of the IEEE JOURNAL OF SOLID-STATE CIRCUITS from 1994 to 1996 and Guest Editor of the July 1992 special issue. From 2000 to 2007 he was a Distinguished Lecturer of the IEEE Solid-State Circuits Society. He was named one of the outstanding contributors for the first 50 years of the ISSCC. He was a corecipient of the Best Student Paper Award at the 2005 Symposium on VLSI.